A Mechanism for Secondary Sea Ice Formation Driven by Double-diffusive Supercooling

Margaret R. Lindeman

October 23, 2019

Abstract

Sea ice forms rapidly in gaps in ice cover, driven by large heat fluxes from the ocean to the atmosphere. The resulting brine rejection forms a cold, salty water mass that sinks and flows away from its source. Here, we present a mechanism for secondary ice formation due to supercooling at the interface between this cold, salty water mass and the relatively fresh mixed layer overlying it. Motivated by Ice-Tethered Profiler (ITP) measurements from the Canada Basin that show the onset and persistence of these conditions, we develop a model for supercooling-driven frazil ice formation that can be generalized to the Arctic or Antarctic. We quantify the contribution of the frazil ice formed through this mechanism to the thickness of the overlying sea ice and the resulting evolution of the mixed layer temperature and salinity fields.

1 Introduction

1.1 Motivation

Sea ice has a key impact on the planetary energy budget, and impacts air-sea exchanges near the poles [1, 16]. In a changing climate, the fate of sea ice is of critical importance, but complicated dynamics make prediction challenging. Sea ice has long posed an impediment to observing ocean properties in the Arctic. Since the mid-2000s, Ice Tethered Profilers (ITPs) have been deployed to mitigate this challenge [15]. ITPs are anchored in sea ice and periodically measure conductivity, temperature, and depth (CTD) profiles of the underlying water column, producing unprecedented year-round hydrographic observations of the ice-covered Arctic Ocean. These measurements provide insight into ocean circulation under sea ice as well as thermodynamic interactions between the sea ice and ocean [14].

Most sea ice growth is driven directly by local surface cooling where the ocean is

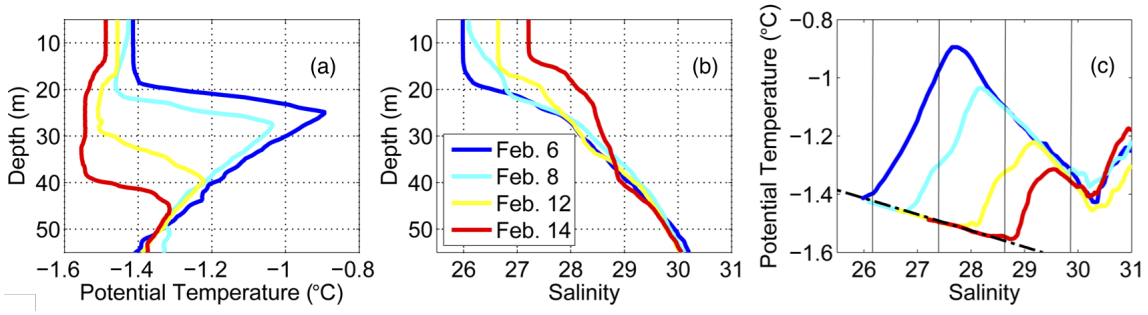

Figure 1: Ice Tethered Profiler observations from the Canada Basin (figure from [13]).

exposed to the atmosphere, such as in polynyas and leads, which are gaps in sea ice cover [8]. As sea ice forms, it excludes salt from its crystal structure, leaving behind very cold, saline water known as brine. The dense brine then sinks until it is neutrally buoyant, and may flow outward from where it formed, intruding beneath the relatively warm and fresh mixed layer insulated by the surrounding sea ice. Some ITP profiles show the arrival of cold, salty water mass at a depth of around 20m (e.g. the transition from the dark blue to red lines in figure 1a-b), which is speculated to be brine generated by this primary ice formation process. Due to the salinity dependence of the freezing point, each of these water masses is at its local freezing temperature (figure 1c). Because heat diffuses faster than salt, as the mixed layer loses heat to the underlying brine, it may become supercooled (figure 2). This could result in the nucleation of ice crystals called frazil ice. However, measuring supercooling directly is difficult, because the instrument itself can act as a nucleus for ice formation. It is desirable to develop a model for this mechanism to identify an observable signature of the process and to quantify its potential for secondary frazil ice production.

1.2 Double-diffusive supercooling

A number of earlier studies utilized theory and laboratory experiments to investigate similar processes related to double-diffusive supercooling. Notably, Martin and Kaufmann's 1974 experimental setup allowed them to describe a three-phase ice growth process that occurs in under-ice melt ponds [5]. In this situation, the meltwater temperature is 0^oC and salinity is 0 g/kg, causing the upper layer to become less dense as it cools (freshwater has a maximum density at 4^oC), which drives convective instability. Stigebrandt (1981) similarly developed a theory where convective instability arises in both layers [11]. Voropayev et al. (1995) build on these earlier results, still considering an overlying layer of purely fresh meltwater but adding turbulence to their model to better reproduce observed quantities of frazil production [17]. Observational results are presented in McPhee et al. (2013), who propose a similar supercooling mechanism. Instead of an intrusion of cold brine on a timescale of days to weeks, they observe a tidally-advected salinity front that is speculated to induce double-diffusive supercooling in a fully turbulent water column [7].

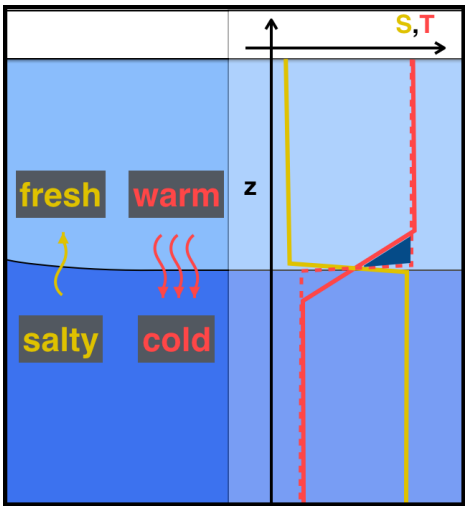

Figure 2: Schematic of double-diffusive supercooling. The initial temperature indicated by the red dashed profile is the salinity- dependent freezing point (right). Because heat diffuses faster than salt (left), after a short time, the temperature in the upper layer has decreased (solid red profile), while the salinity remains at its initial value (yellow profile). The blue triangle represents supercooling of the boundary layer, where the temperature is below the freezing point.

1.3 Frazil ice

Jeffries et al. (1995) measured sea ice cores from the Beaufort Sea and found that 9% of ice thickness was formed from incorporated frazil ice, including layers ranging from 5cm to 60cm thick [2]. They speculate that most of that ice may be attributed to under-ice melt pond growth (see section 1.2), with a plausible alternative being "ice pumps," analogous to those observed in the Antarctic by Langhorne et al. (2015). Ice pumps arise due to the pressure dependence of the freezing point. In the Ross Sea, this happens where deep ice shelves melt and the buoyant meltwater becomes supercooled as it ascends, producing a platelet ice layer up to about 1m thick [4]. Building on these observational studies, modeling studies including Svensson and Omstedt (1994) and Rees Jones and Wells (2017) make significant contributions to understanding the conditions that generate frazil ice and facilitating generalization of supercooling-driven frazil ice growth and the subsequent dynamics to other situations [12, 10].

The aim of this project was to use an idealized model to quantify the parameters affecting the magnitude and persistence of supercooling driven by double-diffusion at the interface between a mixed layer and underlying cold brine water mass, and ultimately quantify the contribution of the resulting frazil ice formation to the thickness of the overlying sea ice.

2 Model

2.1 Model setup

We use an idealized model of supercooling at the base of a well-mixed under-ice layer to simulate a situation similar to the one seen in ITP observations (e.g. figure 1). See figure 3 for a schematic representation of the model setup. The model simulates mixed layer temperature T and salinity S, as well as the number density N and mean radius $\bar{R}$ of ice crystals suspended in the layer. The layer is assumed to be well-mixed, with the temperature and salinity both uniform with depth. The frazil ice crystals are assumed to be disc shaped, with a constant thickness H and variable radius R [6]. The crystals rise through the layer at a velocity proportional to the mean radius, but otherwise there is no flow in the mixed layer.

The initial salinity S_0 of the mixed layer is chosen based on observations, and its initial temperature T_0 is the freezing point determined by its salinity. The underlying cold brine layer will be referred to as the reservoir. The reservoir salinity is assumed to be constant and greater than the mixed layer salinity, and its temperature (also constant) is also at the salinity-dependent freezing point, making the reservoir colder than the mixed layer. The freezing point T_f is assumed to be approximately independent of pressure (i.e. a function of salinity S) and calculated as

$$T_f(S) = T_f(S_0) + \Gamma(S - S_0), \tag{1}$$

where $T_f(S)$ is the freezing temperature at salinity S_0 and $\Gamma = -0.06^oC$ [3]. Mixed layer temperature and salinity are subject to diffusion of heat and salt across the bottom boundary, with diffusivities of heat κ_T and salt κ_S acting across a boundary layer of thickness δ. Under molecular diffusion, $\kappa_T \gg \kappa_S$, but the ratio $\tau = \kappa_T/\kappa_S$ may vary with the level of turbulence.

2.2 Model formulation

To model the ice crystal suspension, we assume a crystal size distribution such that $n(R)$ is the number density of crystals of any given radius R, as illustrated in figure 4. The total number density N is defined as

$$\bar{N} = \int_0^\infty n \mathrm{d}R, \tag{2}$$

measured in units of crystal number per unit volume, and the mean radius $\bar{R}$ as

$$\bar{R} = \frac{1}{N} \int_0^\infty Rn \mathrm{d}R. \tag{3}$$

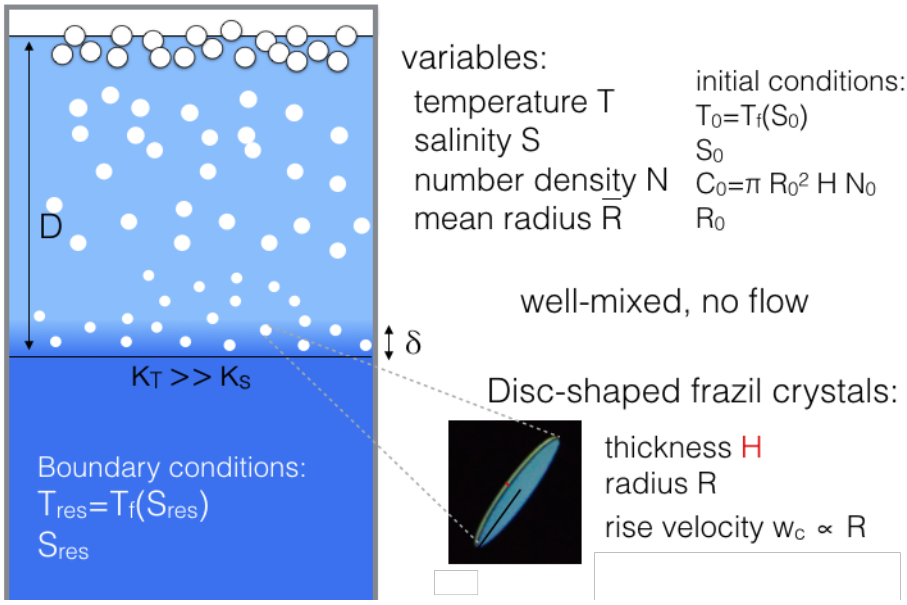

Figure 3: Model schematic and list of variables. Subscript 0 indicates the initial value of a variable. $T_f(S)$ is the salinity-dependent freezing point as defined in (1). C_0 is an initial ice crystal concentration as defined in (10). Ice crystal image from [6].

The rise velocity of disc shaped ice crystals may be parameterized simply with the linear relationship

$$w_c = \gamma R, \tag{4}$$

where the constant $\gamma = 16$ s^{-1} is estimated from experimental data [6, 10].

The time derivative of $n(R)$ can be formulated relatively simply following [10] as

$$\frac{\partial n}{\partial t} = -\frac{\partial}{\partial R}(Gn) - w_c \frac{\partial n}{\partial z}, \tag{5}$$

where $G = G_0\big[T_f(S) - T\big]$ and the growth constant G_0 is defined as

$$G_0 = \frac{\kappa_{Tm}\rho_w c_w}{\rho_i L H}. \tag{6}$$

The first term on the right hand side of (5) is due to crystal growth, which shifts the crystal size distribution $n(R)$ to the right. The second term is the settling of crystals as they rise. In order to model the suspension of ice crystals in a well-mixed layer, we integrate (5) with respect to R and z.

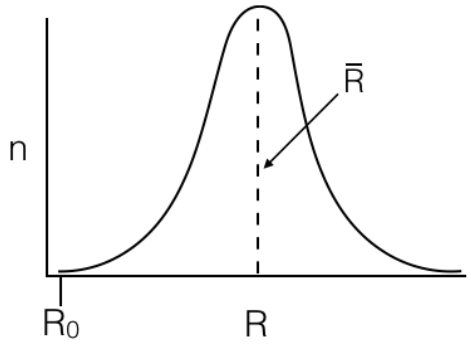

Figure 4: Schematic of crystal size distribution. R_0 is the initial radius and $\bar{R}$ is the mean radius.

This leads to the equation for evolution of the depth-averaged number density N:

$$D\frac{\partial N}{\partial t} = \gamma R_0 N_0 - \gamma \bar{R} N, \tag{7}$$

which is a balance between influx of crystals at the initial radius R_0 and number density N_0 at the base of the mixed layer, and the settling of crystals at the mean radius and number density at the top. This is independent of the growth term because, while crystal growth shifts the size distribution, it has no effect on the total number of crystals.

Because the mixed layer temperature and freezing temperature are assumed to be independent of depth, the supercooling is distributed through the mixed layer and crystals continue to grow radially as they rise. By multiplying (5) by R before integrating, we arrive at an equation for the change in mean radius $\bar{R}$:

$$D\frac{\partial (N\bar{R})}{\partial t} = DG_0\big[T_f(S) - T\big]N + (\alpha+1)\big[\gamma R_0^2 N_0 - \gamma \bar{R}^2 N\big], \tag{8}$$

with mixed layer depth D, latent heat of solidification L, ice density ρ_i, seawater density ρ_w, and molecular diffusivity of heat κ_{Tm}. α is a parameter that accounts for the shape of the crystal size distribution, defined as

$$\alpha \equiv \frac{\int_0^\infty R^2 n \mathrm{d}R}{\bar{R}\int_0^\infty R n \mathrm{d}R}. \tag{9a}$$

The distribution shape determines the relationship between $\bar{R}^2$ and $\overline{R^2}$. If all crystals are the same size (corresponding to a delta function distribution), $\alpha = 0$. Otherwise, $\alpha > 0$. For example, for a Gaussian distribution with standard deviation σ,

$$\alpha \approx \frac{\sigma}{\bar{R}}. \tag{9b}$$

For the purposes of this report, we found the impact of α to be negligible, so henceforth we consider (8) with $\alpha = 0$.

The ice concentration can thus be expressed as the characteristic volume of a crystal times the number of crystals per unit volume:

$$C = \pi \bar{R}^2 H N. \tag{10}$$

The evolution of mixed layer temperature T and salinity S are governed by diffusion of heat and salt across the interface and the addition of salt and latent heat due to the growth of ice crystals:

$$\frac{\partial T}{\partial t} = \frac{L\rho_i}{c_w \rho_w} G_0 [T_f(S) - T] N \bar{R} 2\pi H - \kappa_T \left[\frac{T - T_{\text{res}}}{D\delta} \right], \tag{11}$$

$$\frac{\partial S}{\partial t} = \frac{\rho_i}{\rho_w} G_0 [T_f(S) - T] N \bar{R} 2\pi H S - \kappa_S \left[\frac{S - S_{\text{res}}}{D\delta} \right], \tag{12}$$

with diffusivities of heat and salt κ_S and κ_T reservoir temperature T_{res} and salinity S_{res}.

It is useful to define supercooling θ as

$$\theta = T - T_f(S), \tag{13}$$

choosing a sign convention where negative θ indicates supercooling (i.e. the mixed layer temperature is below the freezing point determined by its current salinity). We can directly compute the evolution of θ as

$$\frac{\partial \theta}{\partial t} = \frac{\partial T}{\partial t} - \Gamma \frac{\partial S}{\partial t}, \tag{14}$$

as we do in our definition of the dimensionless system below, or it can be computed post hoc given the evolution of T and S.

2.3 Dimensionless parameters

We nondimensionalize the variables as

$$\hat{\theta} = \frac{T - T_f(S)}{\Delta T}, \quad \hat{S} = \frac{S}{S_0}, \quad \hat{R} = \frac{\bar{R}}{R_0}, \quad \hat{N} = \frac{DG_0\Delta T}{\gamma R_0^2 N_0} N, \quad \hat{t} = \frac{\kappa_T}{D\delta} t, \tag{15}$$

with ΔT defined as

$$\Delta T = T_f(S_0) - T_{\text{res}}. \tag{16}$$

The timescale we have chosen is the adjustment timescale for cooling of the whole mixed layer depth D by diffusion of heat across the boundary layer δ.

The resulting nondimensional governing equations corresponding to (14), (12), (7), and (8), respectively, can be written as

$$\frac{\partial \hat{\theta}}{\partial \hat{t}} = -2\text{Pe}C_0\hat{N}\hat{R}\hat{\theta}\big[\text{St} - \mathcal{L}\frac{\rho_i}{\rho_w}\hat{S}\big] - \big[\hat{\theta} + \mathcal{L}(\hat{S} - 1) + 1\big] + \mathcal{L}\tau\big[\hat{S} - \hat{S}_{\text{res}}\big], \tag{17a}$$

$$\frac{\partial \hat{S}}{\partial \hat{t}} = -2\text{Pe}C_0\frac{\rho_i}{\rho_w}\hat{N}\hat{R}\hat{\theta}\hat{S} - \tau(\hat{S} - \hat{S}_{\text{res}}), \tag{17b}$$

$$\frac{\partial \hat{N}}{\partial \hat{t}} = -\text{Pe}\hat{R}\hat{N} + \mathcal{G}r, \tag{17c}$$

$$\frac{\partial (\hat{R}\hat{N})}{\partial \hat{t}} = \mathcal{G}r\hat{N}\hat{\theta} - \text{Pe}\hat{R}^2\hat{N} + \mathcal{G}r, \tag{17d}$$

where the six dimensionless parameters are defined as follows:

$$\tau \equiv \frac{\kappa_S}{\kappa_T}, \tag{18a}$$

$$\text{Pe} \equiv \frac{\gamma R_0 \delta}{\kappa_T}, \tag{18b}$$

$$\text{St} \equiv \frac{\rho_i L}{\rho_w c_w \Delta T}, \tag{18c}$$

$$\mathcal{G}r \equiv \frac{G_0 \Delta T \delta D}{\kappa_T R_0}, \tag{18d}$$

$$\mathcal{L} \equiv \frac{\Gamma S_0}{\Delta T}, \tag{18e}$$

$$\hat{S}_{\text{res}} \equiv \frac{S_{\text{res}}}{S_0}. \tag{18f}$$

It is worth briefly explaining the significance of these parameters and their approximate values for the parameter ranges that will be explored in section 3. It is critical to this problem that τ (18a), the ratio of salt diffusivity to heat diffusivity, have a value much less than 1, because that is the origin of the supercooling. The Péclet number Pe (18b) is defined as a ratio of crystal rise velocity to heat diffusion across the basal boundary layer, which has a value on the order of 50, indicating that heat diffuses slowly relative to the timescale on which crystals remain in the suspension. The Stefan number $\mathcal{S}$t (18c) describes the ratio of latent to sensible heat, an indicator of the efficiency of ice production, and is on the order of 10^3. The growth parameter $\mathcal{G}r$ (18d) increases as $\mathcal{S}$t decreases, and describes the relative change in size by crystal growth over the cooling timescale, compared to the initial radius. It is on the order of 10^4, indicating that the timescale of crystal growth is much faster than the timescale of heat diffusion, and crystals will grow substantially. The liquidus number $\mathcal{L}$ (18e) is the ratio of the initial mixed layer freezing temperature to temperature gradient, and is on the order of 20. The scaled reservoir salinity $\hat{S}_{\text{res}}$ is order 1.

3 Results

3.1 Timescales of system evolution

The system of equations (17) is solved numerically to simulate the evolution of the system over 30 days, providing some insight into the basic behavior and important timescales of this system (figure 5). Henceforth, dimensional quantities will be used in the figures and discussion. The initial conditions and parameter values used for this simulation are initial mixed layer salinity $S_0 = 28$ g/kg, reservoir salinity $S_{\text{res}} = 29$ g/kg, temperature gradient $\Delta T = 0.06^o$C, initial concentration $C_0 = 10^{-7}$, initial radius $R_0 = 0.2$mm, and mixed layer depth $D = 10$m. Consistent with previous laboratory and modeling experiments of supercooling and frazil ice formation, the system first cools rapidly, which is accompanied by an explosion in ice concentration (e.g. [9, 10]).

After the time of peak supercooling, which scales as the cooling adjustment timescale discussed earlier,

$$t \sim \frac{D\delta}{\kappa_T}, \tag{19}$$

the magnitude of supercooling shows a small and gradual decrease, along with the ice concentration and mean radius. This change coincides with the salinity increasing approximately linearly with time.

By running the simulation over 500 days (which is unrealistic physically because of the relative ephemerality of these conditions), we can see the full theoretical evolution of

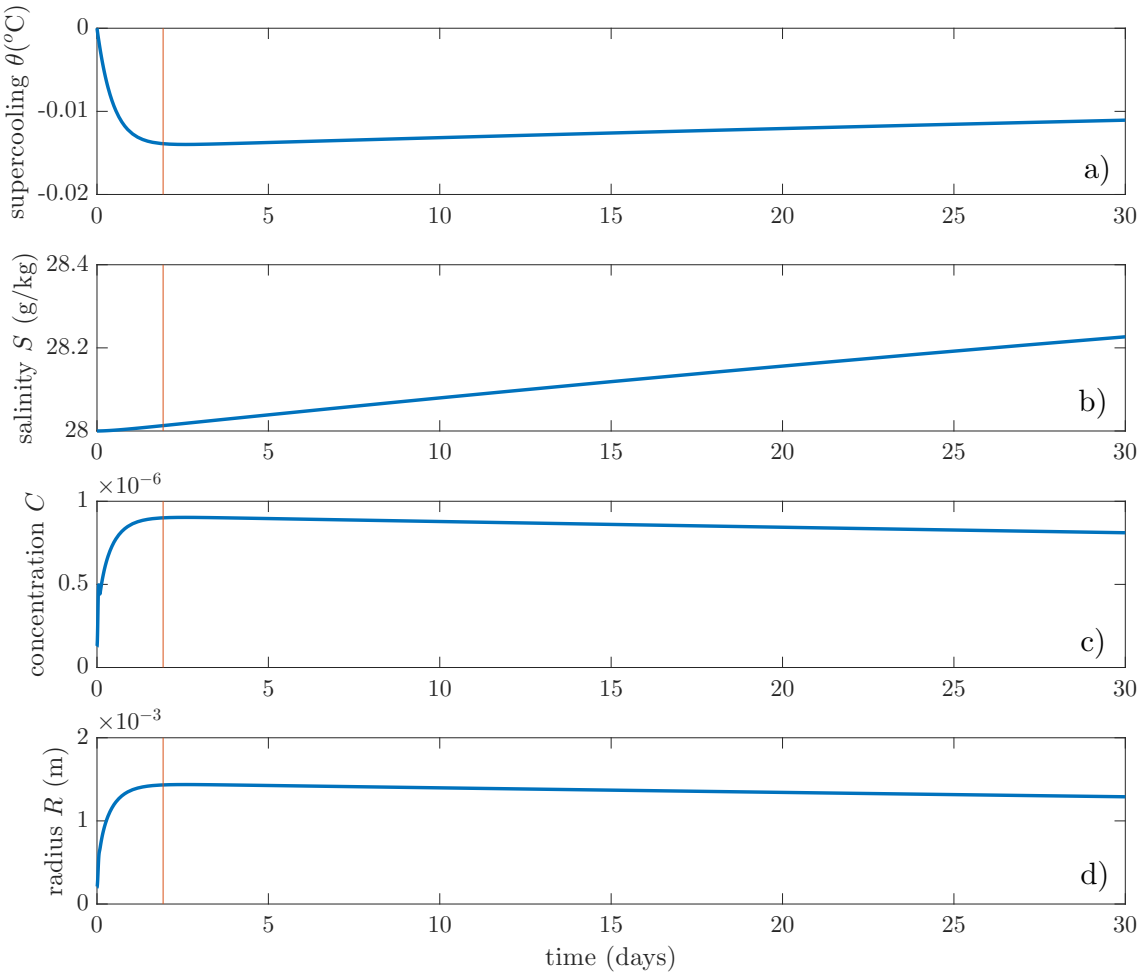

Figure 5: 30-day evolution of mixed layer (a) supercooling θ, (b) salinity S, (c) ice concentration C (10), and (d) mean crystal radius $\bar{R}$. The red line indicates the timescale of peak supercooling (19). The initial conditions used for this simulation are $S_0 = 28$ g/kg, $S_{\text{res}} = 29$ g/kg, $\Delta T = 0.06^o$C, $C_0 = 10^{-7}$, $R_0 = 0.2$mm, and $D = 10$m.

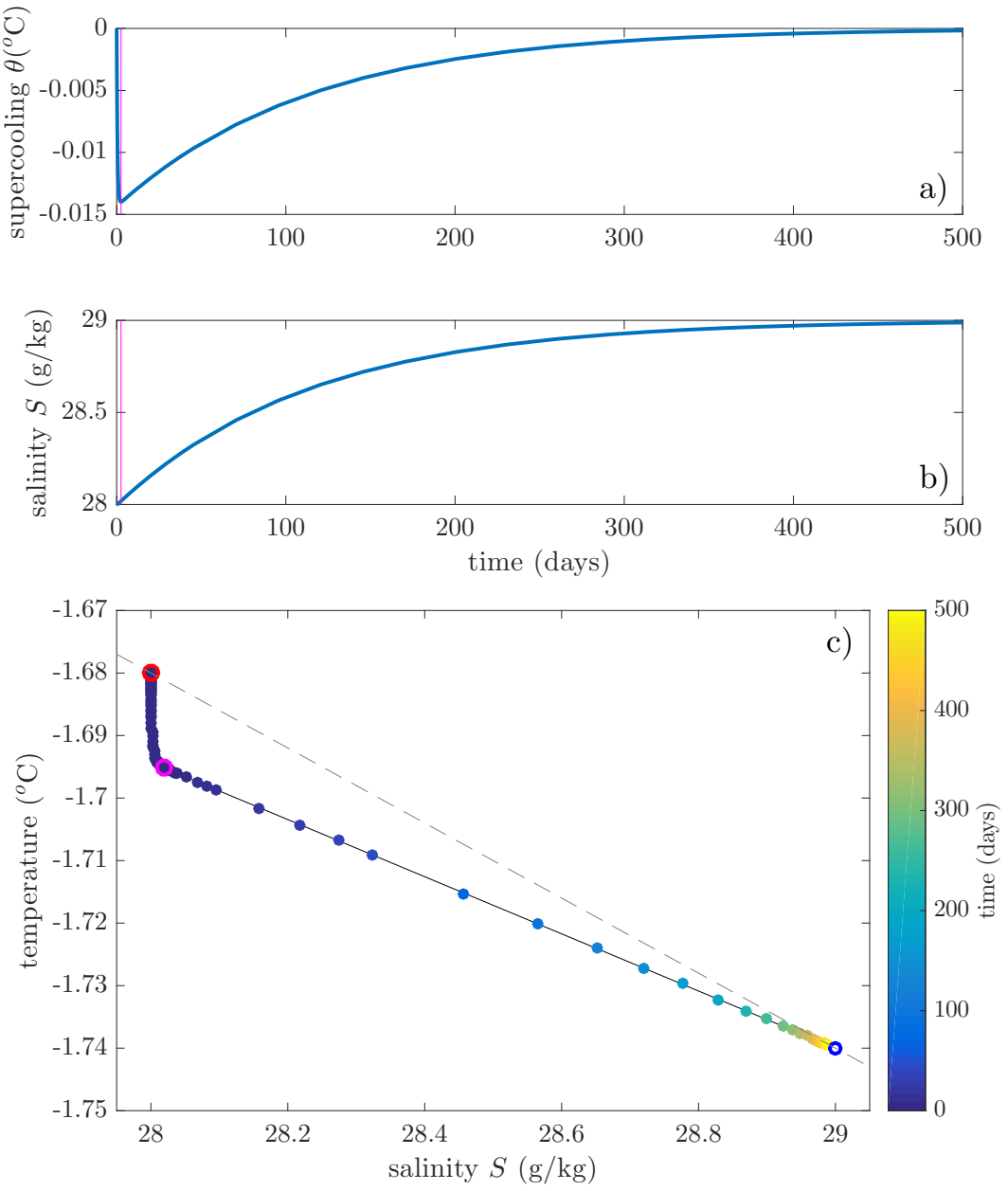

Figure 6: 500-day simulation of mixed layer (a) temperature and (b) salinity. The magenta lines indicate the time of peak supercooling. (c) Points on the T-S plot are colored by day and indicate the mixed layer conditions. The red circle in the T-S plot indicates the initial temperature and salinity of the mixed layer; magenta indicates the magnitude of peak supercooling; blue is the reservoir temperature and salinity. The dashed grey line is the freezing line. Parameter values as in figure 5.

this system in temperature-salinity space (figure 6c). The magnitude of supercooling decreases monotonically after the peak, qualitatively following the salinity (figure 6a-b), although the T-S plot shows that the temperature of the mixed layer continues to decrease, indicating that the slow evolution of the system is driven by the increasing salinity lowering the freezing temperature. The steady decrease in temperature and increase in salinity are qualitatively consistent with the changing temperature and salinity profiles in figure 1.

3.2 Fast evolution

Plotting the time evolution of each variable's time derivative gives some more insight into the initial transient period (figure 7e-h). Prior to the peak supercooling, the supercooling is dominated by the heat flux out of the mixed layer. However, as the ice concentration increases, more latent heat is released into the mixed layer as those crystals grow, and the peak supercooling is reached when those tendencies balance (figure 7e):

$$\frac{L\rho_i}{c_p\rho_w} G_0(T_f - T) N \bar{R} 2\pi H \sim \kappa_T \left[\frac{T - T_{\text{res}}}{D\delta}\right]. \tag{20a}$$

The crystal number density N and mean radius $\bar{R}$ also peak at this point, with the crystals settling out at the top balancing the influx of crystals, and radial crystal growth balancing reduction of the mean radius by precipitation of larger crystals (figure 7g-h), respectively:

$$\gamma \bar{R} N \sim \gamma R_0 N_0 \tag{20b}$$

$$G_0(T_f - T) D N \sim \gamma \bar{R} N \tag{20c}$$

These balances lead to scalings for the peak supercooling,

$$\frac{\theta_{\text{peak}}}{\Delta T} \sim \frac{\beta}{2} \frac{\kappa_T}{D\delta G_0} \frac{\rho_w c_p \Delta T}{\rho_i L} \frac{1}{N_0 R_0 \pi H}, \tag{21a}$$

mean ice crystal radius,

$$\frac{\bar{R}^2_{\text{peak}}}{R_0^2} \sim \frac{\beta}{2} \frac{\kappa_T}{\gamma\delta} \frac{c_p \rho_w \Delta T}{\rho_i L} \frac{1}{N_0 R_0 \pi H}, \tag{21b}$$

and ice concentration,

$$C_{\text{peak}} \sim \frac{C_0}{R_0} \bar{R}_{\text{peak}}, \tag{21c}$$

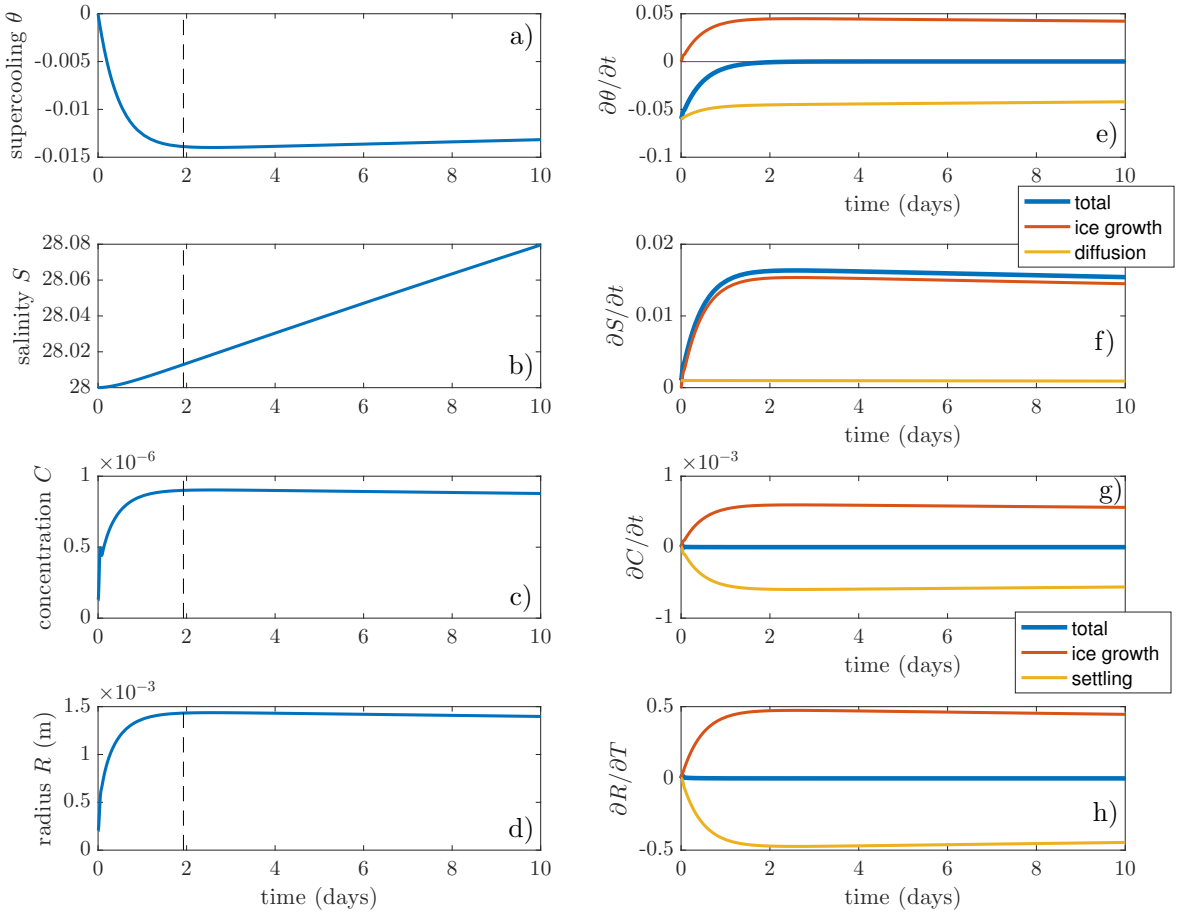

Figure 7: (a-d) Evolution for the first 10 days of the simulation with parameter values as in figure 5 are plotted with the time of peak supercooling indicated by the grey dashed line. (e-h) The associated tendencies are plotted (blue) along with their major constituents (red and yellow). The top legend applies to θ and S; the bottom legend applies to C and $\bar{R}$.

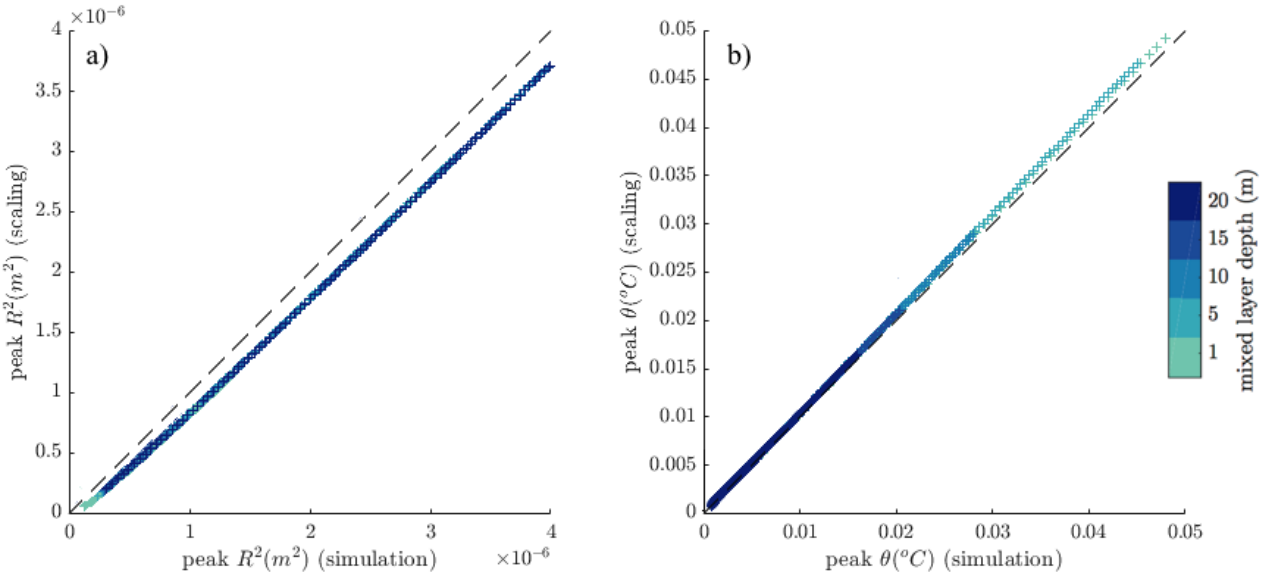

Figure 8: (a) The squared maximum radius $\bar{R}^2$ calculated using (21b) is plotted against the simulated value for a range of values of initial heat flux Q_0 and mixed layer depth D. (b) As in (a), but for peak supercooling θ (21a).

with dimensionless factor β arising from the assumption that $T_f(S) - T_{res} \approx \Delta T$:

$$\beta \equiv \frac{1}{1 + \frac{\kappa_T}{2\pi R_0 H N_0 G_0 D \delta} \frac{c_w \rho_w}{L \rho_i}} = \frac{1}{1 + \frac{1}{\mathrm{St}\, \mathcal{G}r\, C_0}}. \tag{22}$$

These can also be written in terms of the dimensionless parameters (18):

$$\frac{\theta_{\text{peak}}}{\Delta T} \sim \frac{\beta}{2 C_0 \mathcal{G}r \mathcal{S}t}, \tag{23a}$$

$$\frac{\bar{R}^2_{\text{peak}}}{R_0^2} \sim \frac{\beta}{2 Pe \mathcal{S}t C_0} \tag{23b}$$

The scaling $\bar{R}^2_{\text{peak}}$ slightly underestimates the peak radius relative to the simulation (figure 8a), while the θ_{peak} scaling slightly overestimates the magnitude of supercooling (figure 8b), but both are linear with respect to initial heat flux Q_0 and mixed layer depth D.

3.3 Slow evolution

The slow evolution of the system after the time of peak supercooling is driven by increasing salinity due to salt rejection as the ice crystals grow (figure 7f). This depresses the freezing point, reducing the magnitude of supercooling. As a result, the mean ice crystal radius and concentration also decline very gradually.

To get some more insight into this timescale, we can arrive at a scaling estimate using a few simplifications. First, a balance between latent heat release due to ice freezing and cooling due to the heat flux across the boundary is assumed (20a). Second, mean radius and number density are approximated to be constant, with

$$\bar{R}N \approx R_0 N_0. \tag{24}$$

We also require $\tau \ll 1$.

This gives us a leading order balance for $\frac{\partial S}{\partial t}$:

$$\frac{\partial S}{\partial t} \sim \frac{\rho_i}{\rho_w} G_0 \big[T_f(S) - T\big] N \bar{R} 2\pi H S. \tag{25}$$

Defining $T_m = 0^o$C and

$$T_f(S) = T_m + \Gamma S, \tag{26}$$

we can substitute for $T_f - T$ in (25) to get

$$\frac{\partial S}{\partial t} \approx \left(\frac{\lambda\Gamma}{T_{res} - T_m}\right) S \left[S + \frac{T_m - T_{res}}{\Gamma}\right]. \tag{27}$$

Here we have defined a parameter λ, which has units s^{-1}:

$$\lambda \equiv (T_{res} - T_m) \frac{c_p}{L} \frac{\kappa_T}{D\delta} \left[\frac{1}{1 - \frac{1}{N_0 R_0 2\pi H} \frac{\kappa_T c_p}{D\delta G_0 L}}\right]. \tag{28}$$

The solution of (27) yields a scaling for the slow evolution of salinity $S(t)$:

$$S(t) \sim \frac{-T_{res}}{\Gamma} \left(1 + \frac{\Delta T}{\Gamma S_0} e^{-\lambda t}\right)^{-1}, \tag{29}$$

and $\frac{1}{\lambda}$ is an approximate timescale for relaxation of the mixed layer salinity S to the reservoir salinity S_{res} (i.e. the timescale on which supercooling would be depleted if the appropriate conditions persisted).

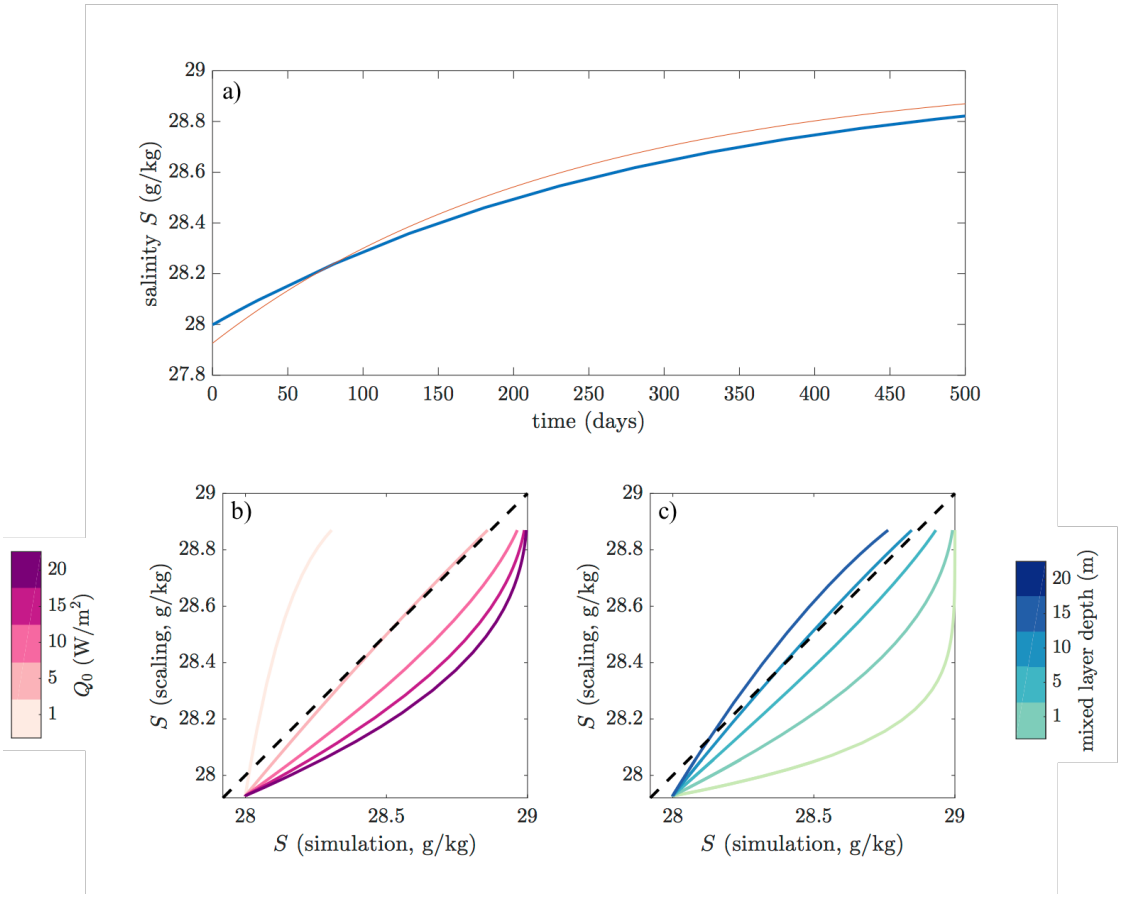

Figure 9: (a) The simulated slow evolution of $S(t)$ over 500 days (blue) is plotted with the scaling estimate from (29) (red) for the baseline initial conditions. (b) The scaling value of the salinity is plotted against the simulation value of the salinity over the 500-day run for a range of values of initial heat flux Q_0. (c) As in (b), but for a range of values of mixed layer depth D.

For the parameter values used in these simulations (see section 3.1), this scaling qualitatively captures the timing and magnitude of mixed layer salinity evolution on long timescales (figure 9a). However, it doesn't apply to all parameter ranges, overestimating salinity for very small heat fluxes and deep mixed layers, and underestimating salinity for large heat fluxes and shallow mixed layers (figure 9b-c).

3.4 Quantifying ice accumulation

We are interested in quantifying the potential contribution to ice thickness resulting from this mechanism. We can define accumulation at each timestep as

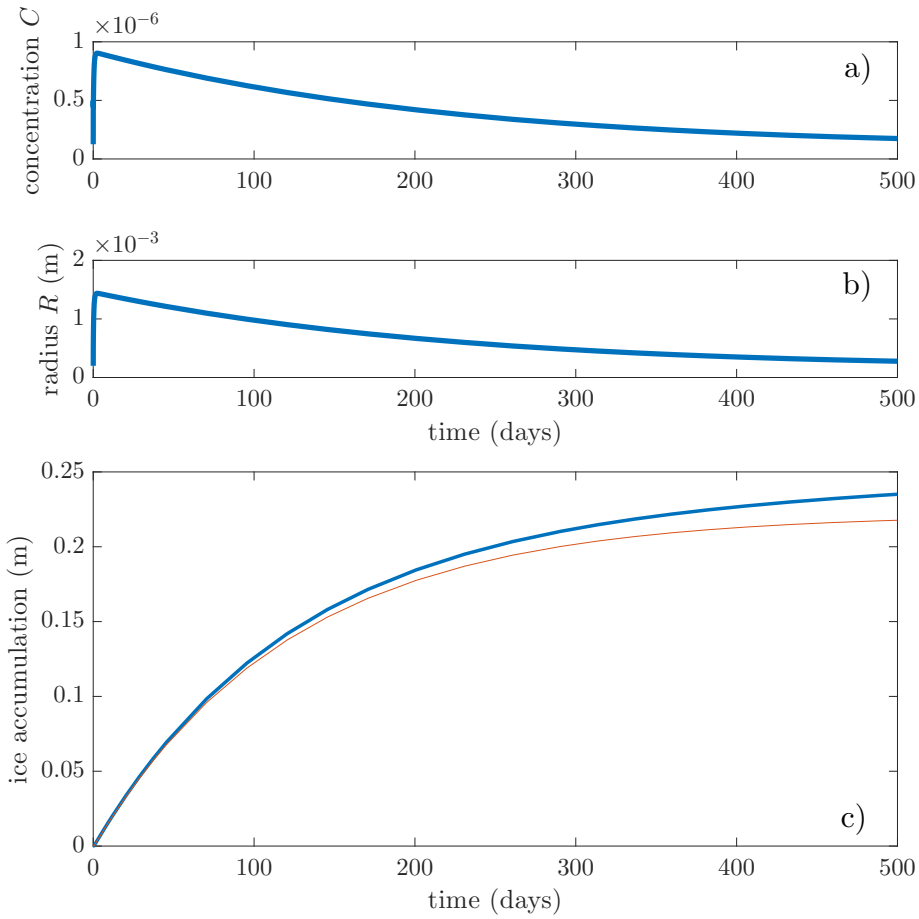

Figure 10: (a-b) Ice concentration C and mean radius $\bar{R}$ are plotted over 500 days. (c) Ice accumulation as calculated in (30) (red) and assuming $(\gamma R_0)\pi R_0^2 N_0 \ll (\gamma \bar{R})\pi \bar{R}^2 HN$ (blue).

$$\frac{\partial h}{\partial t} = (\gamma \bar{R})\pi \bar{R}^2 H N - (\gamma R_0)\pi R_0^2 N_0, \tag{30}$$

where the first term represents settling of ice crystals at the mean radius and the second term removes the contribution of the crystals seeded at the bottom of the mixed layer in the model. We see that for about 100 days of the simulation, the contribution of the second term is negligible (figure 10c). In theory, the system would saturate where these terms were equal, i.e.

$$\frac{\bar{R}^3 N}{R_0^3 N_0} \sim 1, \tag{31}$$

which is where the red curve levels out in figure 10c. However, as discussed previously, these conditions are unlikely to persist for more than a few weeks. On more realistic timescales, we can approximate that N and R are equal to their peak values N_{peak} and R_{peak}, leading us to the scaling

$$\frac{\partial h}{\partial t} \sim \frac{1}{2}\frac{\kappa_T}{\delta}\frac{1}{\mathcal{S}t}, \tag{32a}$$

with $\mathcal{S}t$, defined in (18c), representing the efficiency of ice production relative to cooling at the mixed layer boundary. This is easily solved (and the constants rearranged) to find

$$h(t) \sim \frac{1}{2}\frac{Q_0}{L\rho_i}t, \tag{32b}$$

We find that this is one half of the theoretical upper bound, assuming perfect conversion of cooling to ice production:

$$h_{\max}(t) = \frac{Q}{L\rho_i}t. \tag{33}$$

We test this scaling using a model simulation over 30 days (figure 11a). We find that for small values of Q_0 up to about $10 W/m^2$ and large mixed layer depths of 10-20m, or relatively slow adjustment timescales (19), the scaling estimate (dashed line) agrees qualitatively with the simulated ice production. In general, larger heat fluxes generate more ice production, which is captured by the scaling, but it does not account for the impact of mixed layer depth D. The colors overlaid on the curve for each mixed layer depth show the mean radius $\bar{R}$ at the end of the simulation. Deeper mixed layers have larger $\bar{R}$, indicating that one explanation for the dependence on depth is that ice

crystals in deep layers remain in the supercooled mixed layer longer before settling at the top, facilitating more radial growth and thus greater total accumulation.

The depth dependence is further explained in figure 11b, which shows the peak and final supercooling θ of the mixed layer at various values of D. The greatest magnitude of supercooling is much greater for the 1m mixed layer than for the 20m mixed layer. However, the final magnitude of θ is substantially smaller than the peak for the shallower layer, because the latent heat and salt released by ice freezing in the shallow mixed layer are relatively concentrated and erode the supercooling rapidly. In contrast, the final value of θ in the 20m layer is very close to its peak, and nearly indistinguishable for lower values of Q_0. This is supported by the depletion timescale $\frac{1}{\lambda}$ (28), which is directly related to D and inversely related to $\frac{\kappa_T}{\delta}$. Finally, ice accumulation is also well-correlated with maximum ice concentration C (figure 11c).

In order to compare the values of ice accumulation to frazil ice layer thickness in observational studies, it is necessary to estimate an ice volume fraction. Based on a combination of observational and modeling estimates, this factor is approximated as $\mathcal{T} = 0.25 \pm 0.09$ [4], resulting in a layer thickness around 4 times greater than the accumulation values shown in figures 10c and 11a, or between 1cm and 15cm over 30 days as calculated using (32b) and Q_0 between 1 and 10 W/m^2.

4 Conclusions and Future Work

Our model reaffirms that differing rates of heat and salt diffusion can generate supercooling at the interface between water masses. We have described the evolution of the mixed layer as a result of this process and derived scalings to quantify the effects of system parameters on key quantities, including the peak supercooling, which defines the overall phase-space trajectory of mixed layer properties, and ice crystal radius. We have shown that under realistic Arctic conditions, this mechanism could contribute non-negligible secondary sea ice growth, and identified key parameters that may determine the quantity of ice production.

In order to rigorously quantify the uncertainties, more observations are necessary to constrain appropriate parameter ranges and evaluate the model predictions. We will continue to improve the model, notably by adding depth variation. We also intend to evaluate the potential for convective mixing by the rising ice crystals.

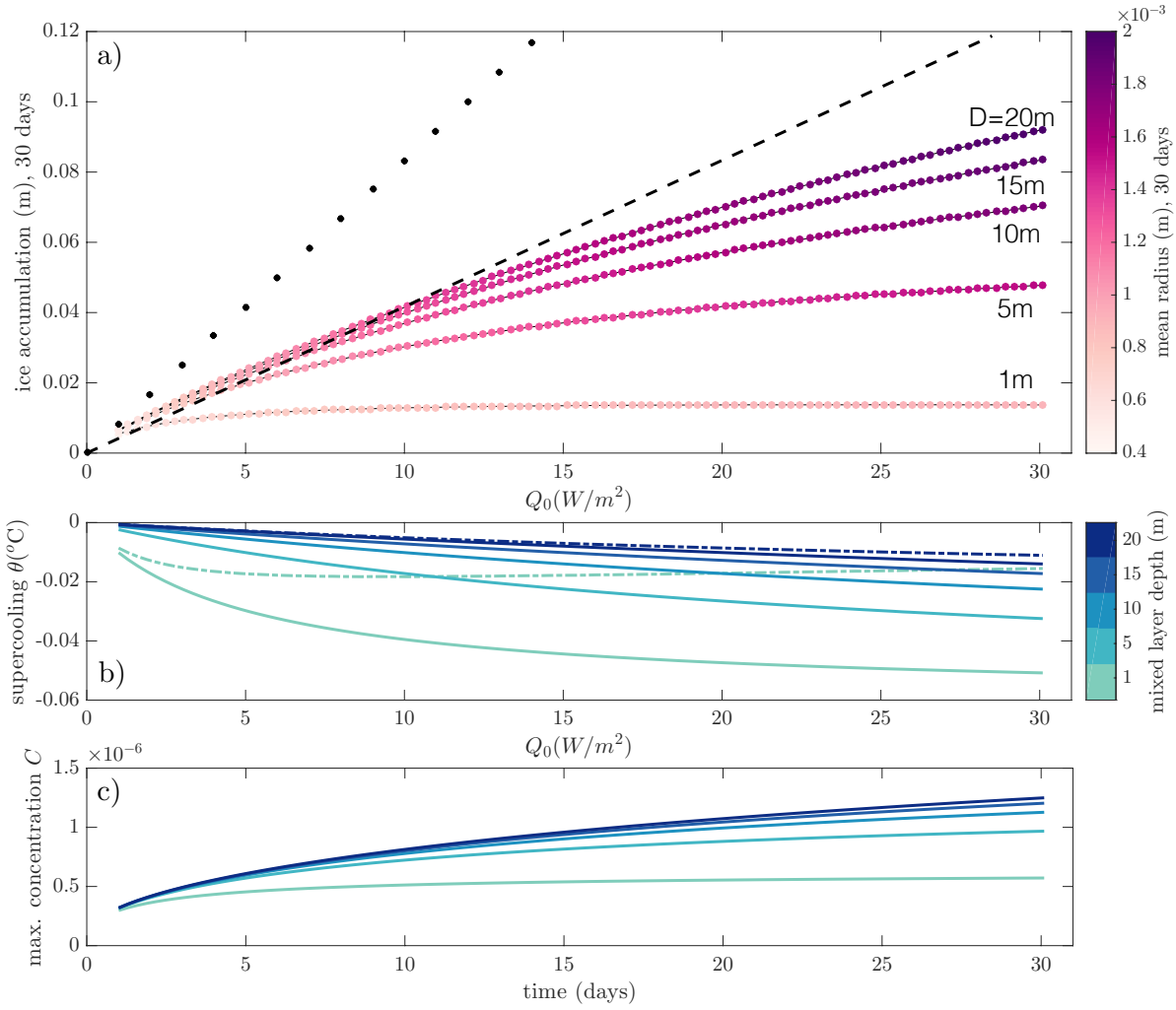

Figure 11: (a) Ice accumulation after 30 days is plotted against initial heat flux Q_0 for different values of the mixed layer depth D (labeled). The color of the dots indicates the mean ice crystal radius $\bar{R}$ after 30 days. The growth scaling law given in (32b) (dashed) and theoretical upper bound for ice accumulation (33) (dotted) are also plotted. (b) Peak supercooling is plotted against initial heat flux Q_0 for different values of the mixed layer depth D (solid lines). The remaining supercooling after 30 days is plotted for the 1m and 20m mixed layer (dashed lines). (c) Maximum concentration C is plotted against initial heat flux Q_0 for different values of the mixed layer depth D.

Acknowledgments

I would like to thank Mary-Louise Timmermans and Andrew Wells for their peerless expertise, generous patience, and boundless good humor in guiding me through this project! I am also grateful to everyone in and around Walsh Cottage who helped me throughout the summer, especially Claudia Cenedese, Craig McConnochie, Renske Gelderloos, Ian Hewitt, Sam Pegler, Bruce Sutherland, Colm-cille Caulfield, Janet Fields, Julie Hildebrandt, Joe Pedlosky, Fiamma Straneo, and the many wonderful visitors. Finally, thanks to the Fellows for sharing many "ups" and a few "downs" but food always.

References

[1] M. I. Budyko, *The effect of solar radiation variations on the climate of the Earth*, Tellus, 21 (1969), pp. 611–619.

[2] M. O. Jeffries, K. Schwartz, K. Morris, A. D. Veazey, H. R. Krouse, and S. Gushing, *Evidence for platelet ice accretion in Arctic sea ice development*, Journal of Geophysical Research: Oceans, 100 (1995), pp. 10905–10914.

[3] A. Jenkins, *Convection-driven melting near the grounding lines of ice shelves and tidewater glaciers*, Journal of Physical Oceanography, 41 (2011), pp. 2279–2294.

[4] P. J. Langhorne, K. G. Hughes, A. J. Gough, I. J. Smith, M. J. M. Williams, N. J. Robinson, C. L. Stevens, W. Rack, D. Price, G. H. Leonard, A. R. Mahoney, C. Haas, and T. G. Haskell, *Observed platelet ice distributions in Antarctic sea ice: An index for ocean-ice shelf heat flux*, Geophysical Research Letters, 42 (2015), pp. 5442–5451. 2015GL064508.

[5] S. Martin and P. Kauffman, *The evolution of under-ice melt ponds, or double diffusion at the freezing point*, Journal of Fluid Mechanics, 64 (1974), pp. 507–528.

[6] V. McFarlane, M. Loewen, and F. Hicks, *Laboratory measurements of the rise velocity of frazil ice particles*, Cold Regions Science and Technology, 106-107 (2014), pp. 120 – 130.

[7] M. G. McPhee, R. Skogseth, F. Nilsen, and L. H. Smedsrud, *Creation and tidal advection of a cold salinity front in Storfjorden: 2. supercooling induced by turbulent mixing of cold water*, Journal of Geophysical Research: Oceans, 118 (2013), pp. 3737–3751.

[8] M. A. Morales Maqueda, A. J. Willmott, and N. R. T. Biggs, *Polynya dynamics: a review of observations and modeling*, Reviews of Geophysics, 42 (2004), pp. 1–37. RG1004.

[9] A. Omstedt and U. Svensson, *Modeling supercooling and ice formation in a turbulent Ekman layer*, Journal of Geophysical Research: Oceans, 89 (1984), pp. 735–744.

[10] D. W. Rees Jones and A. J. Wells, *Frazil-ice growth rate and dynamics in mixed layers and sub-ice-shelf plumes*, The Cryosphere Discussions, 2017 (2017), pp. 1–22.

[11] A. STIGEBRANDT, *On the rate of ice formation in water cooled by a more saline sublayer*, Tellus, 33 (1981), pp. 604–609.

[12] U. Svensson and A. Omstedt, *Simulation of supercooling and size distribution in frazil ice dynamics*, Cold Regions Science and Technology, 22 (1994), pp. 221–233.

[13] M.-L. Timmermans, *The impact of stored solar heat on Arctic sea ice growth*, Geophysical Research Letters, 42 (2015), pp. 6399–6406. 2015GL064541.

[14] M.-L. Timmermans, J. Toole, A. Proshutinsky, R. Krishfield, and A. Plueddemann, *Eddies in the Canada Basin, Arctic Ocean, observed from ice-tethered profilers*, Journal of Physical Oceanography, 38 (2008), pp. 133–145.

[15] J. Toole, R. Krishfield, A. Proshutinsky, C. Ashjian, K. Doherty, D. Frye, T. Hammar, J. Kemp, D. Peters, M.-L. Timmermans, K. von der Heydt, G. Packard, and T. Shanahan, *Ice-tethered profilers sample the upper Arctic Ocean*, Eos, 87 (2006), pp. 434, 438.

[16] T. Vihma, *Effects of Arctic sea ice decline on weather and climate: A review*, Surveys in Geophysics, 35 (2014), pp. 1175–1214.

[17] S. I. Voropayev, H. J. S. Fernando, and L. A. Mitchell, *On the rate of frazil ice formation in polar regions in the presence of turbulence*, Journal of Physical Oceanography, 25 (1995), pp. 1441–1450.